Impact of Ni-based catalyst patterning on hydrogen production from MSR: External steam reformer modelling

Abdelhakim Settar, Zakaria Mansouri, Rachid Nebbali, Brahim Madani, Said Abboudi

Impact of Ni-based catalyst patterning on hydrogen production from MSR: external steam reformer modelling

Abdelhakim SETTAR[a*], Zakaria MANSOURI[b], Rachid NEBBALI[c], Brahim MADANI[c], Said ABBOUDI[d]

[a] INSA Centre Val de Loire, University Orléans, PRISME, EA 4229, F-18020 Bourges, France

[b] CEA, LITEN, DTBH, 38000, Grenoble, France

[c] USTHB- Faculty of Mechanical Engineering and Process Engineering, LTPMP, BP 32 El Alia 16111Bab Ezzouar Algiers, Algeria.

[d] Institut interdisciplinaire Carnot de Bourogne, UMR 6303 CNRS, Université Bourgogne Franche Comté (UBFC), UTBM, site de Sévenans, CEDEX,90010 Belfort, France

*__Corresponding author:__ Abdelhakim SETTAR

Abstract

Wall-coated Methane Steam Reformers (MSR) are commonly used as fuel processing in the hydrogen production chain. In such devices, the catalyst which is generally nickel-based is coated on the walls, and the heat supply influences directly the fuel processing efficiency. In this work, two-dimensional CFD study is carried out to explore an enhancement on MSR thermal behavior. Two configurations in terms of catalyst coating are investigated. The first MSR configuration is equipped with continuous catalytic layer, while in the second, discrete catalyst layers separated by an inert gap are imposed. The effect of the catalyst patterning on the thermal and mass behavior of MSR is discussed. The results show that the MSR

efficiency can be improved by extending the catalytic zone and discretizing the catalyst coating. Comparing to conventional MSR with continuous catalytic layers, enhancement of 28.71 % in CH_4 conversion and 88.574 % in H_2 production is realized by using discretized catalytic layers.

Keywords: Methane steam reforming; Numerical simulation; catalyst patterning; fuel conversion enhancement; hydrogen production.

1. Introduction

Hydrogen (H_2) is considered as one of the most promising energy carriers. It appears to be a potential candidate facing the climatic and environmental issues that our planet earth is confronted. In fact, the most attractive aspect of hydrogen carrier consists on its energetic properties: abundance in the universe; high energetic potential; clean energy carrier and so on. Regarding the abundance of hydrogen, it is not readily available, it is necessary to produce it from available feedstock, such as water. However, the cost of producing H_2 from water is expensive compared to its production from other resources (natural or renewable). Currently, H_2 is produced from fossil fuels and extensive researches and efforts are going on to facilitate its use as a clean energy [1,2].

Several technological procedures and processes are used in the industry to produce H_2 from fossil fuels. Natural gas reforming is by far the most used process, more commonly known as Methane Steam Reforming process (MSR) [3–7]. Many efforts have been made during the last decades to improve the ways of H_2 production. The improvements are intended to: enhance the existing MSR technologies [8,9], perform new designs for MSR systems [10,11] and develop new materials and composites [12,13]. Note that the reformers are classified according to their position in Fuel Cell (FC) systems. From one hand, the reforming system can be internal where the H_2 is produced in the FC [14–16]. In this class of reformers, the major focus of researches and developments concerns High Temperature Fuel Cells (HTFC) using Nickel (Ni) materials as anode or catalyst [17–20]. From the other hand, the reforming system can be also external where H_2 is produced separately and then injected in the FC [21,22].

The intensification of MSR systems can substantially save energy and it is a mean to preserve the environment. The concept of intensification and optimization of the MSR process

represents one of the major concerns of researchers. In fact, this process is often limited by the heat and mass transfer behaviors in the reactors, which sometimes leads to a slow reaction kinetics [23] characterized by the presence of cold spots [24] in the catalytic zones. Thus, many authors have worked extensively to promote the MSR process by: investigating its integration with chemical plants (i.e. ammonia production [25]), developing new FC nanomaterials [26,27], investigating numerous fuels [28,29], studying the catalyst material and its effectiveness [30–33] and designing new reactors configurations and other ways of heat supply [34,35].

Among all the ways cited above for the intensification of MSR, the catalyst materials and reactor geometry are the most issues treated in the literature. Regarding the catalyst material, it is said before that the Ni-based catalyst is the most utilized because it is cost-effective and efficient [36]. The effectiveness factor of this material is the key parameter for the intensification of MSR. It is defined as the ratio of current reaction rate to the reaction rate that would result if entire catalyst interior is exposed to the external surface (called the washcoat) conditions [37]. Baek et al. [31] and Nam [32] have recently studied the effectiveness factors of Ni catalyst pellets under small-scale MSR conditions near atmospheric pressure and then proposed simple correlation equations. Areum et al. [33] estimated the effectiveness factors of Ni washcoat catalyst layers under small-scale MSR conditions. De Jong et al., [38] have focused their attention on the numerical analysis of thermal behavior and the kinetics of the steam reforming reaction of natural gas in a vapo-reformer, to produce hydrogen. They explored the methane conversion performance of six different designs, such as reformer insulation. They showed that a 9.5% improvement in hydrogen production can be achieved by increasing the air fraction by around 50%. In addition, by increasing the thickness of the insulation of the reaction chamber, an additional

improvement of 11.2% can be achieved by promoting the good distribution of heat. Vigneault and Grace [39] designed a prototype of a multi-channel membrane reactor for small-scale production of hydrogen by methane steam reforming. The authors compared their measurements to numerical results. They showed that thanks to this prototype, a methane conversion rate of the order of 87% is reached with a very high hydrogen purity (99.999%). Note that the authors of this study considered a multichannel reactor to obtain 87 % of enhancement, while, in our work only one channel was considered in simulation

Concerning the reactor geometry, several efforts are devoted to optimize the MSR rector configuration in order to intensify the MSR process. Lee et al. [34] integrated a planar heat exchanger steam reformer with a catalytic combustor in order to deliver the unused energy of the anode off-gas for heating and reforming. They investigated the effect of several parameters on both the thermal behavior between the reactors and H_2 volume fraction at the exit of the reformer. Kang et al. [40] investigated the performance of methane conversion in an innovative coupled reactor (combustor and reformer) over variations of operation parameters. Jinwon et al. [7] developed experimentally four MSR rectors having a shell and tube configuration. They examined the effect of heat transfer on the methane conversion performance at low temperature. Their results show that the overall heat transfer area is a critical parameter in achieving a high methane conversion rate.

In this work the effect of the heat supply and configuration of a wall-coated MSR on the methane conversion efficiency is examined using Computational Fluid Dynamics (CFD). Two wall-coated MSR configurations at industrial operating conditions are compared in terms of methane conversion and hydrogen production. The results show that, by applying an intermediate heating of the gas mixture, the cold spots in the reformer are minimized leading to improved heat transfer behavior and thus the methane conversion efficiency.

2. Numerical details

2.1. Geometric model and grid

A parallel-plate catalytic channel is modeled using two-dimensional simulations, where the upper and lower plates are coated with Ni-based catalyst [41], as shown in Figure 1. The MSR channel length and height are 20 mm and 3.1 mm respectively. Two models are proposed, the first is “Model A” and the second is “Model B”. The difference between these models is the segmentation of the catalytic zone within the MSR channel. For the Model A, the catalytic zone (2 catalytic walls) is continuous and takes a 4 mm length. It is positioned at 8 mm away from both the channel inlet and outlet. For the Model B, the catalytic zone (4 catalytic walls) is discontinuous and discretized in two zones; each catalytic zone has a length of 2 mm. These two zones are separated with an inert zone of 2 mm, which leads to an overall length of the catalytic zone of 6 mm. The overall catalytic zone of the model B locates at 7 mm away from both the inlet and outlet of the domain. Note that the thickness of the non-catalytic and catalytic walls is neglected and not considered during the calculations.

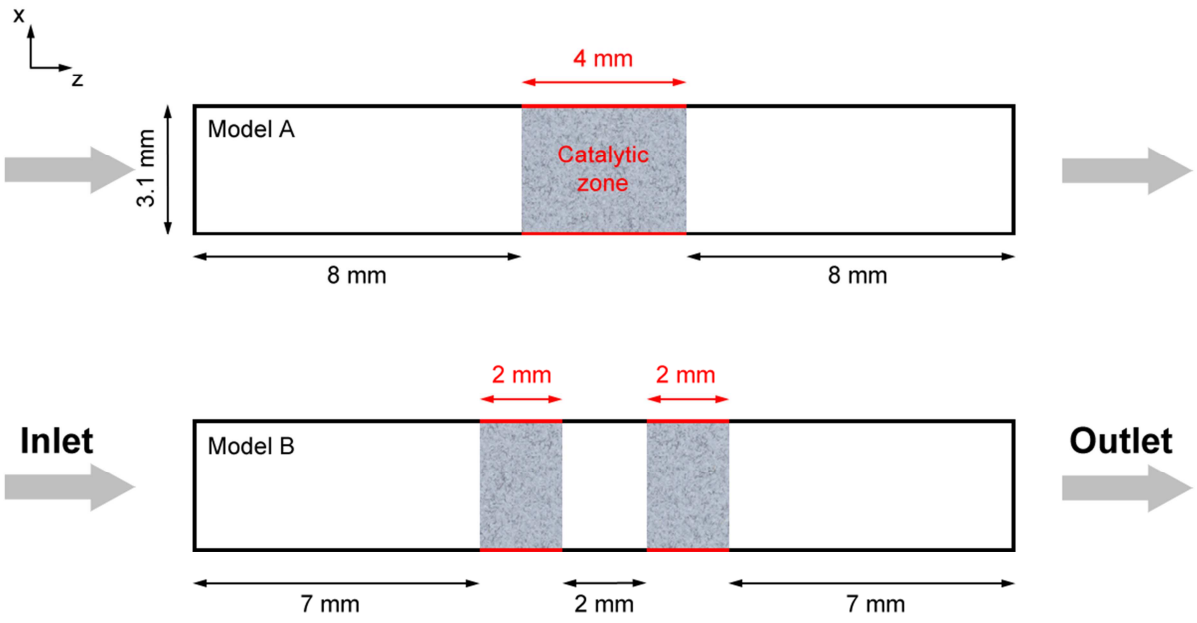

Figure 1. Schematic of the studied configuration “Model A” and Model B” with dimensions in mm

A structured grid with quadrilateral cells is generated for the computational domain. It is non-uniform along both directions and refined near the walls due to the flow gradients at these regions.

2.2. Governing equations

The following assumptions are made: (1) steady-state reactive flow; (2) two-dimensional flow; (3) no gas radiation; (4) laminar flow (low velocity 0.1 m/s); (5) ideal gases and incompressible flows. With the above assumptions, the conservation equations are written as follow:

Continuity

$$\frac{\partial(\rho_{mix}u_x)}{\partial x^g}+\frac{\partial(\rho_{mix}u_z)}{\partial z}=0 \tag{1}$$

x-Momentum

$$\left(u_x\frac{\partial(\rho_{mix}u_x)}{\partial x}+u_z\frac{\partial(\rho_{mix}u_x)}{\partial z}\right)=-\frac{\partial P}{\partial x^g}+\left[\frac{\partial}{\partial x^g}\left(\mu_{mix}\frac{\partial u_x}{\partial x^g}\right)+\frac{\partial}{\partial z}\left(\mu_{mix}\frac{\partial u_x}{\partial z}\right)\right]-K\,u_x \tag{2}$$

z-Momentum

$$\left(u_x\frac{\partial(\rho_{mix}u_z)}{\partial x}+u_z\frac{\partial(\rho_{mix}u_z)}{\partial z}\right)=-\frac{\partial P}{\partial x^g}+\left[\frac{\partial}{\partial x^g}\left(\mu_{mix}\frac{\partial u_z}{\partial x^g}\right)+\frac{\partial}{\partial z}\left(\mu_{mix}\frac{\partial u_z}{\partial z}\right)\right]-K\,u_z \tag{3}$$

Energy equation in the gas-phase

$$u_x\frac{\partial\left(\rho_{mix}C_pT_j^g\right)}{\partial x^g}+u_z\frac{\partial\left(\rho_{mix}C_pT^g\right)}{\partial z}=\frac{\partial}{\partial x^g}\left(\lambda_{mix}\frac{\partial T^g}{\partial x}\right)+\frac{\partial}{\partial z}\left(\lambda_{mix}\frac{\partial T^g}{\partial y}\right)+S_{WGS} \tag{4}$$

Species equation in the gas-phase

$$u_x \frac{\partial(\rho_{mix} w_i^g)}{\partial x^g} + u_z \frac{\partial(\rho_{mix} w_i^g)}{\partial z} = \frac{\partial}{\partial x^g}\left(D_i \frac{\partial \rho_{mix} w_i^g}{\partial x^g}\right) + \frac{\partial}{\partial z^g}\left(D_i \frac{\partial \rho_{mix} w_i^g}{\partial z}\right) \quad (5)$$

Energy equation in the catalytic wall

$$\frac{\partial T^{cat}}{\partial x^{cat}} = -\frac{\sum R_{SMR} \Delta H_i}{\lambda_{mix}} \quad (6)$$

Species equation in the catalytic wall

$$\frac{\partial w_i}{\partial x^{cat}} = -\frac{R(v_i'' - v_i')M_i}{(\rho\, D_i)_{mix}} \quad (7)$$

2.2.1. Gas mixture

The physical properties of gas mixture depend on both mass fraction w_i and temperature. The gas mixture is assumed to be ideal. So, since the gas mixture is assumed to be compressible, the mixture density is obtained by the equation of state for ideal gas:

$$\rho_{mix} = \frac{P}{R_g T^g}\left(\sum_i \frac{w_i^g}{M_i}\right)^{-1} \quad (8)$$

where P_{tot} is the total pressure which is equal to atmospheric pressure; M_{mix} is molar mass of gas mixture, while R_g and T is constant of ideal gases and temperature respectively.

The heat capacity is calculated at constant pressure as function of temperature variation:

$$C_{p_{mix}} = \sum_{i=1}^{n} w_i \,.\, (a + bT + cT^2 + dT^3 + fT^4)_i \quad (9)$$

The thermal conductivity λ_{mix} and dynamic viscosity μ_{mix} of gas mixture are calculated from kinetic theory [40]. Their expressions are as follows:

$$\lambda_{mix} = \sum_{i=1}^{n} \frac{y_i \lambda_i}{\sum_{j=1}^{n} A_{ij} y_j} \quad (10)$$

$$\mu_{mix} = \sum_{i=1}^{n} \frac{y_i \mu_i}{\sum_{j=1}^{n} A_{ij} y_j} \quad (11)$$

with

$$A_{ij} = \omega \left[1 + \left({}^{\mu_i}/_{\mu_j} \right)^{1/2} \left({}^{M_i}/_{M_j} \right)^{1/4} \right]^2 \Bigg/ \left[8(1 + {}^{(M_i}/_{M_j}) \right]^{1/2} \quad (12)$$

where y_i is the molar mass of i_{th} component and A_{ij} is a function obtained using the Mason-Saxena expression [41]. In this formulation, $\omega = 1.065$ for thermal conductivity, while in the basis of the Wilke's method [44], it equals to unity for dynamic viscosity.

Finally, the diffusion coefficient is calculated based on Lewis number. This number is assumed to be unity for all species. It involves that the molecular diffusion is equal to the thermal one. So, the diffusion coefficient is given as follows:

$$D_i = \left(\frac{\lambda}{\rho \, C_p} \right)_{mix} \quad (13)$$

2.2.2. Catalyst wall

The catalytic layer is a mixture of nickel and AL_2O_3. It is modeled using 1D model due to its thin thickness where the diffusion is neglected. One considers that the MSR process occurs only at the surfaces impregnated by nickel-based catalyst. Basing on this assumption, the mass flow of the gas mixture is equals to that at the catalyst interface [45].

2.2.3. Chemical kinetics and reaction rate evaluation

The evaluation of the reaction rate from the MSR kinetics is needed to determine the gas mixture composition between the inlet and the outlet of the MSR. Even the reaction mechanism of MSR involves several elementary reactions; its reaction rate depends of three main reversible reactions: (1) MSR (endothermic reaction); (2) WGS (moderate exothermic reaction) and (3) the reverse methanation (endothermic reaction). The reactants CH_4 and H_2O generate three products with different stoichiometric coefficients at equilibrium state: CO, H_2 and CO_2 by following equation (14):

$$\alpha \, CH_4 + \beta \, H_2O \leftrightarrow \gamma CO + \delta \, H_2 + CO_2 \quad (14)$$

with

$$[\alpha, \beta, \gamma, \delta, \varepsilon] = [-1, -1, +1, +3, 0], [0, -1, -1, +1, +1] \; and \; [-1, -2, 0, +4, +1] \quad (15)$$

for MSR, WGS and reverse methanation reaction respectively. In this work, only the MSR reaction is studied where its enthalpy of reaction is $\Delta H°_{298} = 165 \; [\mathrm{KJ \cdot mol^{-1}}]$. The reaction rate expression considered in this work is based on the power law form and given as follow [14,46–48]:

$$r = A \cdot \left(P_{CH_4}\right)^{0.47} \cdot \left(P_{H_2O}\right)^{-0.01} \cdot exp\left(-\frac{E}{R_g T}\right) \quad (15)$$

where *r* is the specific reaction rate [mol. s^{-1}. g^{-1}], *A*, P_{CH_4} and P_{H_2O} are respectively the pre-exponential factor, partial pressure of reactants. These parameters represent the reaction constant *k* which is monitored by the reaction order coefficients which are determined at atmospheric pressure, 0.47 and -0.01 for CH_4 H_2O partial pressures respectively. The partial pressures of reactants are variable as function of their respective mass fractions, while A is equal to 0.39 $[\mathrm{mol \, . g^{-1}. \, s^{-1}. \, Pa^{-0.46}}]$. *E* is the activation energy of MSR which is equal to $4.32 \times 10^4 \; [\mathrm{J. mol^{-1}}]$.

2.3. Operating and boundary conditions

The MSR channel operates under atmospheric pressure and a prefect mixing of the reactants. The boundary conditions are imposed as follow: the mixture enters the channel with a uniform axial velocity $u_z = 0.1 \, m/s$ and a constant temperature $T^0 = 520 \, °C$. The uniform axial velocity is used here in order to replicate the experiment [41], where the flow was corrected using a porous media. The mass fractions of the species at the inlet are: $w^0_{CH4} = 0.07$, $w^0_{H2O} = 0.29$ and $w^0_{N2} = 0.64$. At the exit of the channel all the axial gradients are set to zero $\partial w_i^g / \partial z = \partial T^g / \partial z = \partial u_z / \partial z$. For all the walls, a non-slip condition is applied $u_z = u_x = 0 \, m/s$ with no species diffusion. A constant temperature equals to the

inlet mixture temperature is applied to the inert walls. At the catalytic walls, Neumann condition is applied using the equations (6) and (7) for the temperature and species calculations, respectively.

2.4. Simulation method

CFD is a powerful tool for simulating fluid flows and related physics. It offers a great benefit to the development of several engineering areas, such as: turbomachinery [49,50], automobile [51], bio-engineering [52], reactive processes [49,53,54] and aerospace [55]. Thus, the simulations of the present study were performed using an in-house CFD code. The code uses the finite-volume method to solve the governing equations. The simulations of the present study were performed using an in-house CFD code which is based on finite-volume method to solve the governing equations. The Semi-Implicit Method for Pressure-Linked Equations (SIMPLE) algorithm is applied for the pressure-velocity coupling. It is a widely used numerical procedure to solve the Navier-Stokes equations due to its easy implementation and quick convergence for a large variety of problems. A power-law scheme is used to solve the 8 transport equations of the mixture applied in the gas-phase and catalyst layer, which are: 1 for pressure, 2 for momentum, 1 for energy and 4 for all species. Before starting the calculations, the flow field in the entire domain is initialized using the values of the inlet. Convergence criteria are set to 10^{-9} for all equations. Further details about the numerical methods used in the code and its validation can be found in our previous works [56,57].

3. Results and discussions

Here we present and discuss the computations obtained after resolution form both configurations. The main objective is to evaluate the performance of SMR equipped with

continuous and discrete catalyst layers to bring to the forefront the effect of the catalyst layer patterning. The efficiency is evaluated by calculating conversion and production rates of methane and hydrogen respectively. They are obtained by integrating the local mass flow as function of the MSR height, *e*, at the outlets (z=L), with inlet mass flow as reference (z=0). Thus, the conversion and production rates X_i are evaluated by following this expression:

$$X_i = 1 - \frac{\int_0^e \rho u_z w_i dx \,|_{z=L}}{\int_0^e \rho u_z w_i dx \,|_{z=0}} \qquad i = CH_4, H_2 \tag{9}$$

Before that, the thermal and CH_4/H_2 mass profiles distribution is presented. Then, a comparison in terms of local quantities is carried out. Finally, we finish by the calculations of CH_4/H_2 conversion/production rates and we quantify the enhancement realized.

1.1. Temperature distribution:

Figure 2 illustrates the thermal behavior within the SMR for both models (A) and (B). Note that the temperature distribution, after and before the catalytic zone, is almost the same for both cases. However, near the catalytic zone the temperature distribution differs significantly from one case to the other. This difference is due to the distribution of the catalyst layers at the lower and upper walls of each model. One can see that the temperature decreases at the catalyst layers, this behavior is caused by the endothermic reaction, which occurs at these locations and leads to the consumption/production of the involved species. Consequently, a considerable amount of heat is absorbed resulting in the decrease of the temperature. The decrease is around half the temperature (250°C) of the mixture at the inlet. Furthermore, downstream the catalyst layers, the temperature increases to reach its initial value (520°C) due to the exchange with the heated walls. Regarding the temperature at the center of the catalytic zone, it takes the values of 390 °C

and 450 °C for the models A and B respectively. The gap between the two catalyst layers (model B) increases the length of the catalytic zone (6mm). This ensures a good heat supply for the mixture to recover the needed heat for the endothermic reaction. From this comparison we can conclude that the model B is better than the model A regarding the heat supply capacity that contributes to an effective CH_4 conversion, as will be shown next.

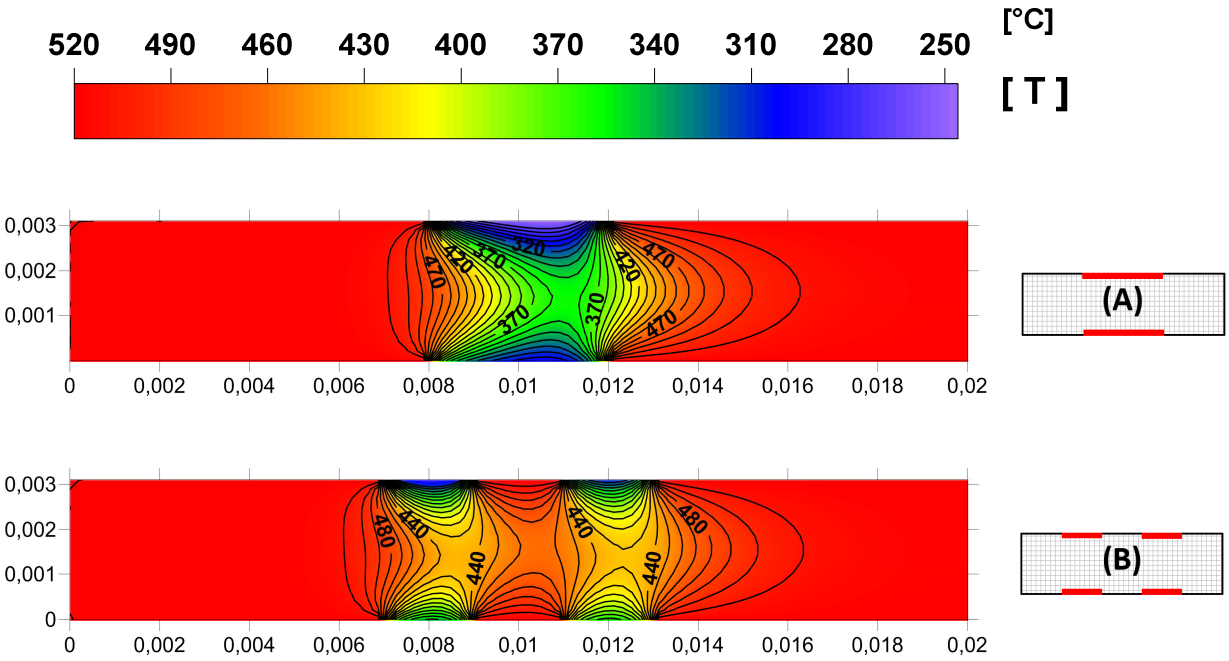

Figure 2. Temperature distribution and contours of MSR models.

1.2. CH_4 and H_2 distributions:

The mass fractions of CH_4 and H_2 within the SMR are shown in Figures 3 and 4 respectively and discussed in this subsection. The distributions of the species for each model are in adequacy with the thermal distributions (Figure 2). For the CH_4, it is consumed when it enters the catalytic zone, as expected. Comparing both models, the model B consumes the CH_4 faster than the model A. For example, the iso-line w_{CH4}=0.13 locates at the average position z=0.011 for the model A, whereas it is located upstream this position for the model B, at around z=0.009. At the outlet, only 43.62% of CH_4 is consumed by configuration A while

it reaches 72.33 % by configuration B. This proves the capability of the proposed model B in consuming significantly the methane to convert it to hydrogen. For the H_2, it is known and clearly seen that form Figure 4 that its production relates directly to the CH_4 consumption. The model B produced more hydrogen that the model A as expected. A. For example, the iso-line w_{H2}=0.055 locates at the average position z=0.011 for the model A, whereas it is located upstream this position for the model B, at around z=0.008. At the outlet, the hydrogen mass fraction reaches its maximum value of 0.06 for the model A, whereas its maximum values for the model B is 0.085. Thus, the model B is more efficient than the model A by 30% of H_2 production. Furthermore, one can observe that by looking to the iso-mass fractions. For example, 38 % of CH_4 amount is converted before the end of the catalytic region for model (A), while, the CH_4 conversion is faster for model (B) where, at the same position (z=11 mm), 57.14 % is converted. Thus, one can conclude that most of fuel is consumed before the mixture leaves the reactor. At the outlet, only 43.62% of CH_4 is converted by configuration (A) while it is about 72.33 % by configuration (B). This behavior enhances the CH_4 non-converted amount at the outlet leading to poor efficiency, more particularly by model (A).

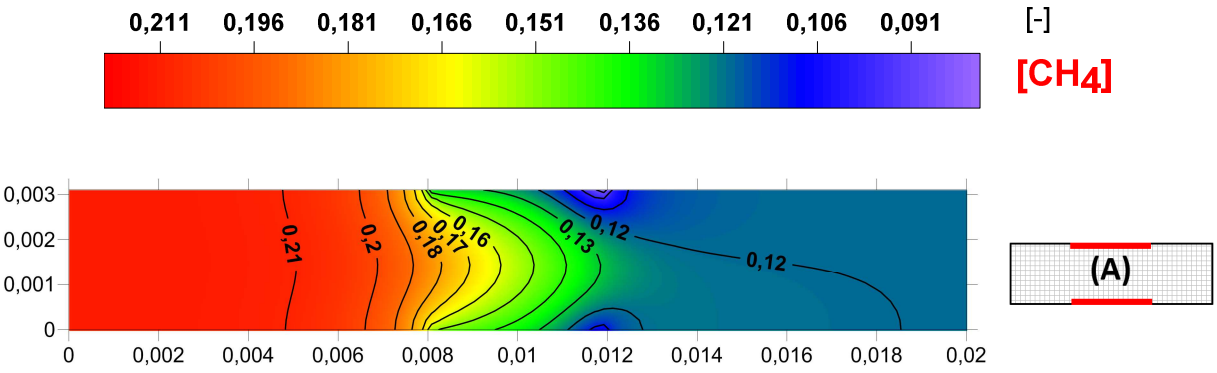

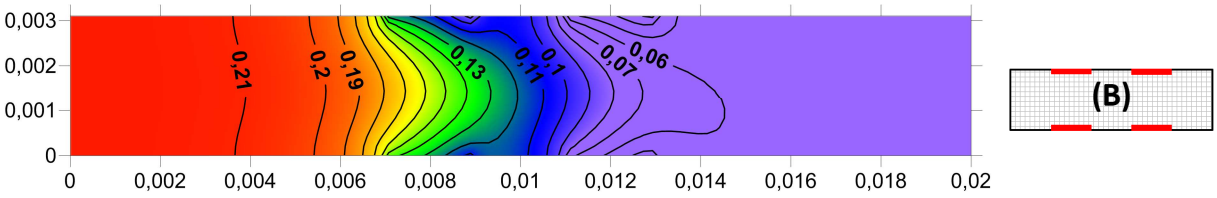

Figure 3. CH_4 mass fraction distribution and contours of MSR models.

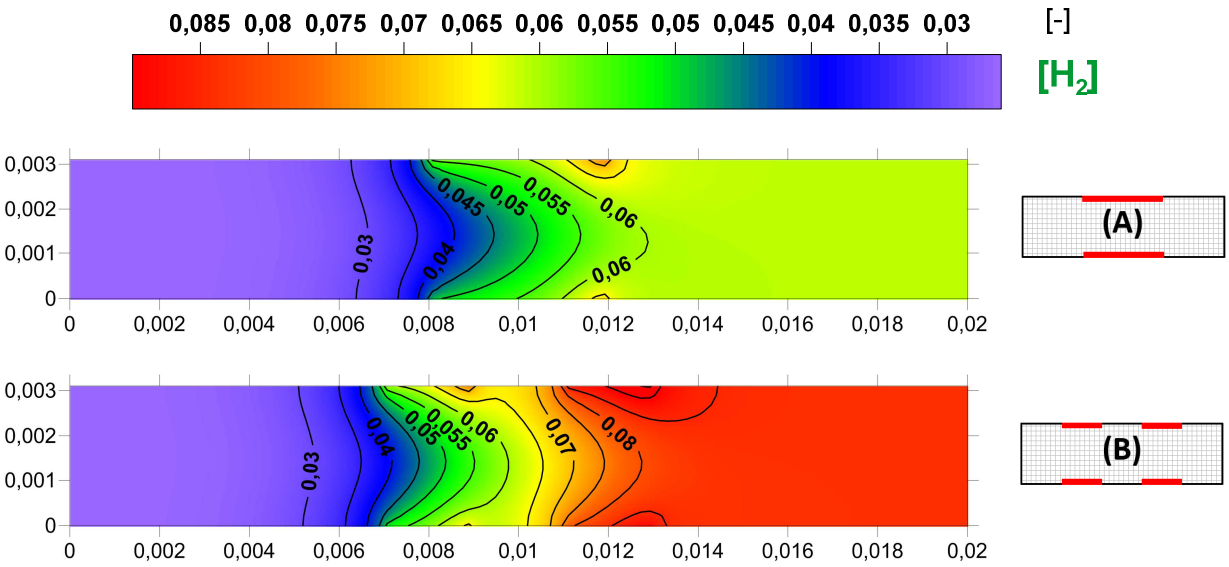

Figure 4. H_2 mass fraction distribution and contours of MSR models.

1.3. Comparison between Model (A) and Model (B):

The above mentioned and discussed contours (Figures 2, 3 and 4) give a general comparison between the models A and B. However, a detailed comparison is needed to investigate the effect of the catalyst arrangement. To this purpose, line comparison of the above quantities is of interest to further assessing the SMR's performance.

a. Average temperatures:

Figure 5 presents the temperature profiles at the channel centerline for both models A and B. At the entrance of SMR (0 < z < 5mm), the temperature profiles remain constant, as

expected from both models due to the absence of reaction in this region. Within the catalytic zone, the temperature profiles behave differently, the model A profile presents one minimum whereas the model B profile shows two minima. Each behavior of these profiles corresponds to the catalyst arrangement. The minima of the model A profile are located at around z = 11 mm and takes the value of 340 °C, while, concerning the model B profile are located at around z = 8 mm and z = 12 mm respectively with almost the same value of 420 °C. For the model A, the reaction process manifests continuously along the catalytic layer, which leads to the consumption of 35% (520-340/520) of the initial temperature within the centerline region. For the model B, the endothermic reaction manifests discontinuously along the catalytic layers. This leads to the consumption of 20% (520-420/520) of the initial temperature at each layer. It is interesting to point out that the consumption rate of the second layer is the same as the first layer due to the presence of the inert wall between the layers. This wall supplies the second layer with more heat (475 °C), which favors the endothermic reaction with a similar manner as the first layer. Note that both profiles reach back the initial temperature again at the channel outlet due to the heat exchange between the mixture and the heated walls.

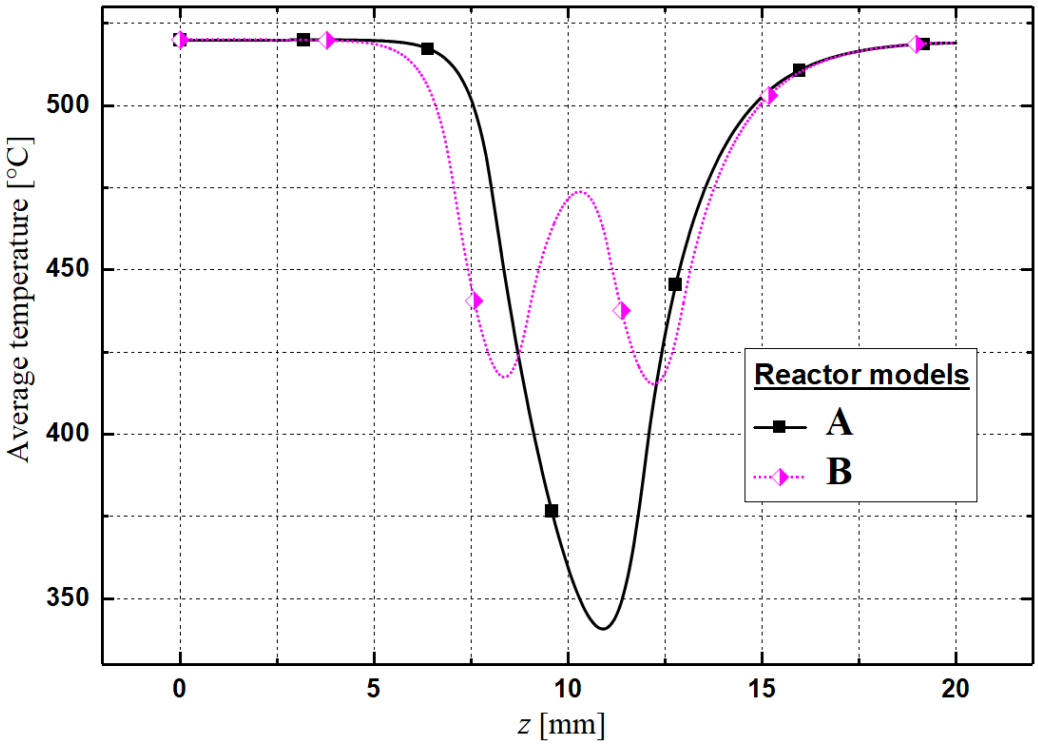

Figure 5. Comparison of the average temperatures, along the SMR models.

b. *Average CH_4 and H_2 mass fractions:*

Figure 6 depicts the evolution of CH_4 and H_2 average mass fractions for Model (A) and (B) (Figure 6(a) and Figure 6(b) respectively). For both models, one observes that the consumption of CH_4 and the production of H_2 behaves the same trends. However, from the beginning of the catalyst zone, noticeable discrepancies between both models are noted for CH_4 consumption as much as for H_2 production. Model (B) equipped by shifted catalyst layer presents best CH_4 consumption along the catalyst zone. This consumption is stronger as the gas mixture crosses the catalyst zone until a minimum CH_4 mass fraction is reached. For Model (B), the lower CH_4 average mass fraction is about 6% around the ending edge (z= 15 mm), while, it is about 12 % using a continuous catalytic layer: enhancement of 50 % in terms of CH_4 consumption is realized. This behavior is certainly due to the thermal behavior.

As remarked in Figure 5, the average temperature is kept higher by shifting the catalytic layer. So, improved and regular heat supply allowed efficient fuel conversion leading to a good yield of H_2. Using model (B), an improvement of 80 % is achieved comparing to model (A) with continuous catalytic layer.

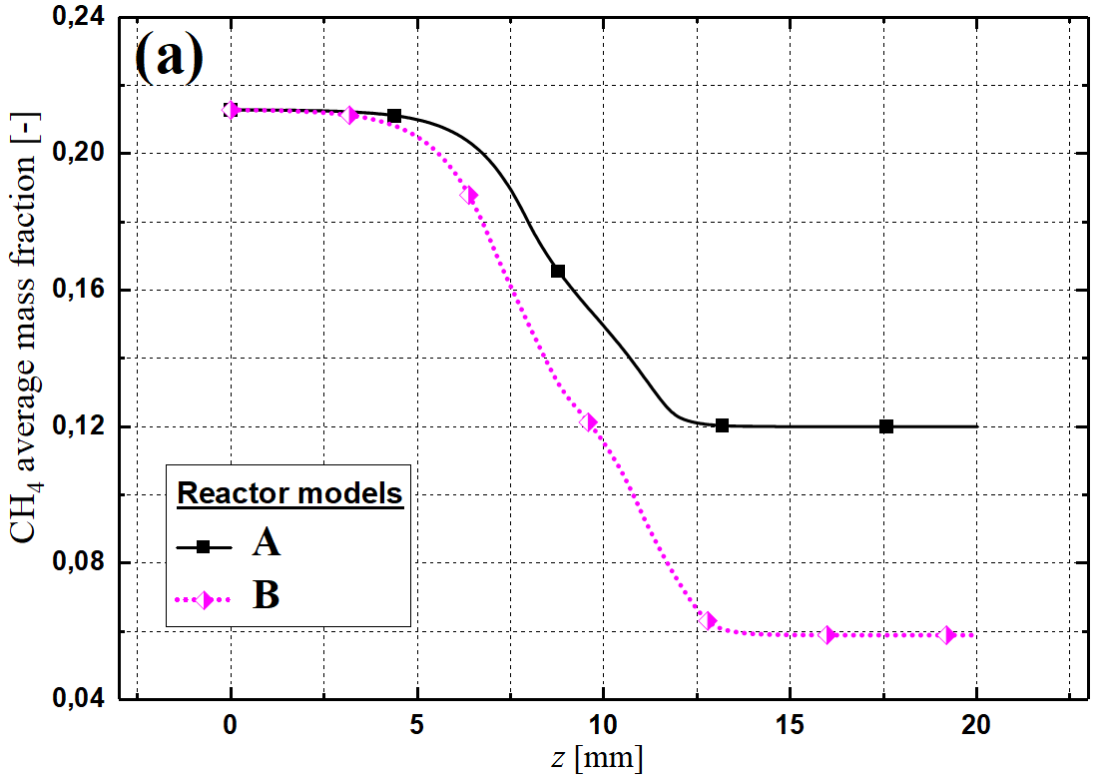

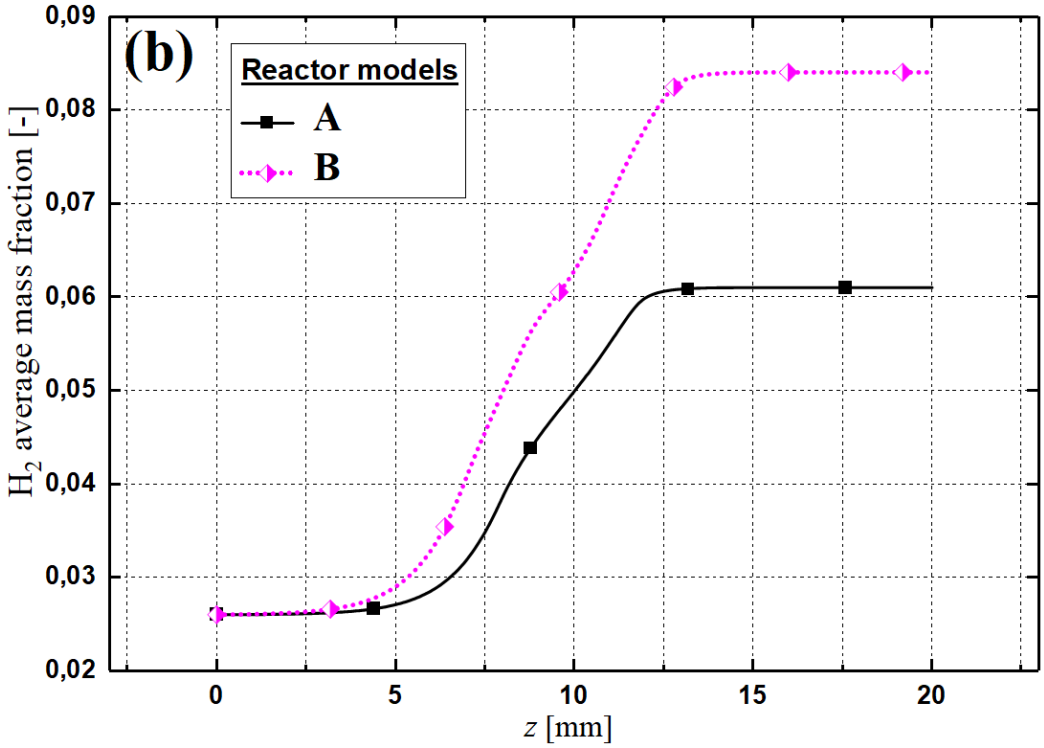

Figure 6. Average mass fraction in MSR models as function of z-axis:

(a) CH_4, **(b)** H_2

1.4. MSR efficiency: conversion and production rates:

Table 4 recapitulates the MSR reaction achievement for the compared models: (1) Inlet species mass fractions (CH_4, H_2O, CO and H_2); (2) Conversion (CH_4) and production (H_2) rates. The reformer efficiency is evaluated by comparing the achievement of each model in terms of conversion and production rates. By looking to CH_4 and H_2 rates, one can conclude that the model (A) gives the weakest performance. By this catalytic layer design, the catalyst is extended to 4 mm without inter-catalytic spacing, only 9.28% of CH_4 is converted leading to significant loss of fuel. By contrast, model (B) achieves good performances even in terms of conversion or production, with a large gap comparing to model (A). CH_4 outlet mass fraction obtained by model (B) is about 5.88 %. Nevertheless, by comparing model (B) with model (A), 6.6 % of additional CH_4 mass fraction is converted which corresponds to 2.3% more H_2 mass fraction.

Table 4. MSR reaction achievement of studied WCR models.

SMR models	**Reactant mass fractions**				**Product mass fractions**				**CH_4 conversion rates [%]**	**H_2 production rates [%]**
	Inlet		**Outlet**		**Inlet**		**Outlet**			
	CH_4	H_2O	CH_4	H_2O	H_2	CO	H_2	CO		
A	21.28	71.45	11.997	61.023	2.6	1.19	6.100	17.401	43.625	134.618
B			5.887	54.161			8.403	28.069	72.335	223.192

Figure 7 outlines the conversion and production rate of CH_4 and H_2. As highlighted in Table 4, model (B) realizes the best overall performance. Basing on the CH_4 and H_2 inlet mass fractions, CH_4 conversion rate of model (B) is about 72.335 % and its H_2 production rate is

about 223.192%. Therefore, compared to model (A), enhancement of 28.71 % in CH_4 conversion and 88.574 % in H_2 production is realized.

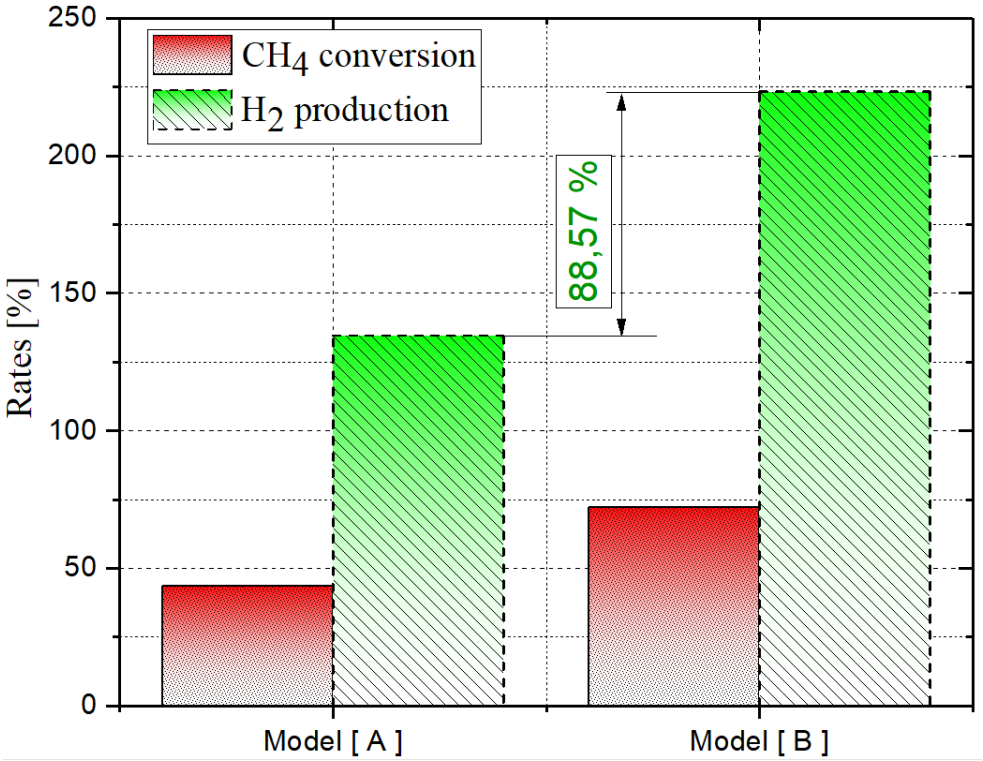

Figure 7. CH_4/H_2 conversion/production rates obtained by each WCR model.

4. Conclusion

The intensification of the Methane Steam Reforming (MSR) process is investigated numerically in a 2D parallel-plate catalytic channel. Two configurations are investigated, "Model A" and "Model B". The Model A contains a single catalytic zone of 4 mm and the Model B contains two discretized zones of 2 mm for each one and separated with an inert layer of 2 mm.

Comparisons between the both models show that the discrete layers (Model B) have superior thermal performances due to the efficient fuel conversion. With Model B, enhancement of 28.71 % in CH_4 conversion and 88.574 % in H_2 production is achieved.

It can be concluded that the MSR efficiency can be improved by segmenting the catalytic zone into subzones in order to extend the catalyst coating. This leads to increase the residence time of the reactants across the reformer and increase the H_2 production rate.

As a perspective, it is interesting to investigate the number of the discretized catalytic layers and the length of inert layer to better optimize the MSR system.

References

[1] Abdalla AM, Hossain S, Nisfindy OB, Azad AT, Dawood M, Azad AK. Hydrogen production, storage, transportation and key challenges with applications: A review. Energy Conversion and Management 2018;165:602–627.

[2] Stern AG. A new sustainable hydrogen clean energy paradigm. International Journal of Hydrogen Energy 2018;43:4244–4255.

[3] Consonni S, Viganò F. Decarbonized hydrogen and electricity from natural gas. International Journal of Hydrogen Energy 2005;30:701–18. doi:10.1016/j.ijhydene.2004.07.001.

[4] Settar A, Abboudi S, Madani B, Nebbali R. Estimation of transient heat flux density during the heat supply of a catalytic wall steam methane reformer. Heat Mass Transfer 2018;54:385–91. doi:10.1007/s00231-017-2131-3.

[5] Murphy DM, Manerbino A, Parker M, Blasi J, Kee RJ, Sullivan NP. Methane steam reforming in a novel ceramic microchannel reactor. International Journal of Hydrogen Energy 2013;38:8741–8750.

[6] Kim C-H, Han J-Y, Lim H, Lee K-Y, Ryi S-K. Methane steam reforming using a membrane reactor equipped with a Pd-based composite membrane for effective hydrogen production. International Journal of Hydrogen Energy 2018;43:5863–5872.

[7] Yun J, Cho K, Lee YD, Yu S. Four different configurations of a 5 kW class shell-and-tube methane steam reformer with a low-temperature heat source. International Journal of Hydrogen Energy 2018;43:4546–62. doi:10.1016/j.ijhydene.2018.01.069.

[8] Xu Y, Ma Y, Demura M, Hirano T. Enhanced catalytic activity of Ni3Al foils towards methane steam reforming by water vapor and hydrogen pretreatments. International Journal of Hydrogen Energy 2016;41:7352–7362.

[9] Naseri AT, Peppley BA, Pharoah JG. A systematic parametric study on the effect of a catalyst coating microstructure on its performance in methane steam reforming. International Journal of Hydrogen Energy 2015;40:16086–16095.

[10] Butcher H, Quenzel CJ, Breziner L, Mettes J, Wilhite BA, Bossard P. Design of an annular microchannel reactor (AMR) for hydrogen and/or syngas production via methane steam reforming. International Journal of Hydrogen Energy 2014;39:18046–18057.
[11] Shin G, Yun J, Yu S. Thermal design of methane steam reformer with low-temperature non-reactive heat source for high efficiency engine-hybrid stationary fuel cell system. International Journal of Hydrogen Energy 2017;42:14697–707. doi:10.1016/j.ijhydene.2017.04.053.
[12] Ali S, Al-Marri MJ, Abdelmoneim AG, Kumar A, Khader MM. Catalytic evaluation of nickel nanoparticles in methane steam reforming. International Journal of Hydrogen Energy 2016;41:22876–22885.
[13] Hirano T, Xu Y. Catalytic properties of a pure Ni coil catalyst for methane steam reforming. International Journal of Hydrogen Energy 2017;42:30621–30629.
[14] Brus G. Experimental and numerical studies on chemically reacting gas flow in the porous structure of a solid oxide fuel cells internal fuel reformer. International Journal of Hydrogen Energy 2012;37:17225–34. doi:10.1016/j.ijhydene.2012.08.072.
[15] Smorygo O, Mikutski V, Marukovich A, Vialiuha Y, Ilyushchanka A, Mezentseva N, et al. Structured catalyst supports and catalysts for the methane indirect internal steam reforming in the intermediate temperature SOFC. International Journal of Hydrogen Energy 2009;34:9505–14. doi:10.1016/j.ijhydene.2009.09.079.
[16] Sohn S, Baek SM, Nam JH, Kim C-J. Two-dimensional micro/macroscale model for intermediate-temperature solid oxide fuel cells considering the direct internal reforming of methane. International Journal of Hydrogen Energy 2016;41:5582–5597.
[17] Shaikh SP, Muchtar A, Somalu MR. A review on the selection of anode materials for solid-oxide fuel cells. Renewable and Sustainable Energy Reviews 2015;51:1–8.
[18] Frattini D, Accardo G, Moreno A, Yoon SP, Han JH, Nam SW. Strengthening mechanism and electrochemical characterization of ZrO2 nanoparticles in Nickel–Aluminum alloy for Molten Carbonate Fuel Cells. Journal of Industrial and Engineering Chemistry 2017;56:285–291.
[19] Frattini D, Accardo G, Moreno A, Yoon SP, Han JH, Nam SW. A novel Nickel-Aluminum alloy with Titanium for improved anode performance and properties in Molten Carbonate Fuel Cells. Journal of Power Sources 2017;352:90–98.
[20] Inoue Y, Hara K, Okudaira K, Ito H, Ninomiya Y, Namioka T. The effect of ceria content in nickel–ceria composite anode catalysts on the discharge performance for solid oxide fuel cells. International Journal of Hydrogen Energy 2018;43:2394–2401.
[21] Kushi T. Performance and durability evaluation of dry reforming in solid oxide fuel cells. International Journal of Hydrogen Energy 2016;41:17567–17576.
[22] Sengodan S, Lan R, Humphreys J, Du D, Xu W, Wang H, et al. Advances in reforming and partial oxidation of hydrocarbons for hydrogen production and fuel cell applications. Renewable and Sustainable Energy Reviews 2018;82:761–780.
[23] Wang F, Qi B, Wang G, Li L. Methane steam reforming: Kinetics and modeling over coating catalyst in micro-channel reactor. International Journal of Hydrogen Energy 2013;38:5693–5704.
[24] Ma R, Castro-Dominguez B, Dixon AG, Ma YH. CFD study of heat and mass transfer in ethanol steam reforming in a catalytic membrane reactor. International Journal of Hydrogen Energy 2018;43:7662–7674.

[25] Frattini D, Cinti G, Bidini G, Desideri U, Cioffi R, Jannelli E. A system approach in energy evaluation of different renewable energies sources integration in ammonia production plants. Renewable Energy 2016;99:472–482.
[26] Abdalla AM, Hossain S, Azad AT, Petra PMI, Begum F, Eriksson SG, et al. Nanomaterials for solid oxide fuel cells: A review. Renewable and Sustainable Energy Reviews 2018;82:353–368.
[27] Fan L, Zhu B, Su P-C, He C. Nanomaterials and technologies for low temperature solid oxide fuel cells: recent advances, challenges and opportunities. Nano Energy 2017.
[28] Matsuka M, Shigedomi K, Ishihara T. Comparative study of propane steam reforming in vanadium based catalytic membrane reactor with nickel-based catalysts. International Journal of Hydrogen Energy 2014;39:14792–14799.
[29] Chen J, Yan L, Song W, Xu D. Comparisons between methane and methanol steam reforming in thermally integrated microchannel reactors for hydrogen production: A computational fluid dynamics study. International Journal of Hydrogen Energy 2018;43:14710–14728.
[30] Zhang X, Peng L, Fang X, Cheng Q, Liu W, Peng H, et al. Ni/Y2B2O7 (BTi, Sn, Zr and Ce) catalysts for methane steam reforming: On the effects of B site replacement. International Journal of Hydrogen Energy 2018;43:8298–8312.
[31] Baek SM, Kang JH, Lee K-J, Nam JH. A numerical study of the effectiveness factors of nickel catalyst pellets used in steam methane reforming for residential fuel cell applications. International Journal of Hydrogen Energy 2014;39:9180–92. doi:10.1016/j.ijhydene.2014.04.067.
[32] Nam JH. Effectiveness factor correlations for spherical nickel catalyst pellets used in small-scale steam methane reformers. International Journal of Hydrogen Energy 2015;40:5644–5652.
[33] Jeong A, Shin D, Baek SM, Nam JH. Effectiveness factor correlations from simulations of washcoat nickel catalyst layers for small-scale steam methane reforming applications. International Journal of Hydrogen Energy 2018;43:15398–15411.
[34] Lee K, Yun J, Ahn K, Lee S, Kang S, Yu S. Operational characteristics of a planar steam reformer thermally coupled with a catalytic burner. International Journal of Hydrogen Energy 2013;38:4767–4775.
[35] Giaconia A, de Falco M, Caputo G, Grena R, Tarquini P, Marrelli L. Solar steam reforming of natural gas for hydrogen production using molten salt heat carriers. AIChE Journal 2008;54:1932–1944.
[36] Rostrup-Nielsen JR. Production of synthesis gas. Catalysis Today 1993;18:305–324.
[37] Rawlings JB, Ekerdt JG. Chemical reactor analysis and design fundamentals. Nob Hill Pub.; 2002.
[38] De Jong M, Reinders AHME, Kok JBW, Westendorp G. Optimizing a steam-methane reformer for hydrogen production. International Journal of Hydrogen Energy 2009;34:285–92. doi:10.1016/j.ijhydene.2008.09.084.
[39] Vigneault A, Grace JR. Hydrogen production in Multi-Channel Membrane Reactor via Steam Methane Reforming and Methane Catalytic Combustion. International Journal of Hydrogen Energy 2015;40:233–43. doi:10.1016/j.ijhydene.2014.10.040.
[40] Kang S, Lee K, Yu S, Lee SM, Ahn K-Y. Development of a coupled reactor with a catalytic combustor and steam reformer for a 5 kW solid oxide fuel cell system. Applied Energy 2014;114:114–123.

[41] Lin KK, Saito M, Niina Y, Ikemura K, Iwai H, Yoshida H. Deduction of Proper Reaction Rate of Steam Methane Reforming over Catalyst Surface Validated with a Combination of One- and Two-Dimensional Simulations. Journal of Thermal Science and Technology 2012;7:633–48. doi:10.1299/jtst.7.633.
[42] Poling BE, Prausnitz JM, O'connell JP. The properties of gases and liquids. vol. 5. McGraw-Hill New York; 2001.
[43] Mason EA, Saxena SC. Approximate formula for the thermal conductivity of gas mixtures. Physics of Fluids (1958-1988) 1958;1:361–369.
[44] Wilke CR. A viscosity equation for gas mixtures. The Journal of Chemical Physics 1950;18:517–519.
[45] Irani M, Alizadehdakhel A, Pour AN, Hoseini N, Adinehnia M. CFD modeling of hydrogen production using steam reforming of methane in monolith reactors: Surface or volume-base reaction model? International Journal of Hydrogen Energy 2011;36:15602–15610.
[46] Lee AL, Zabransky RF, Huber WJ. Internal reforming development for solid oxide fuel cells. Ind Eng Chem Res 1990;29:766–73. doi:10.1021/ie00101a009.
[47] Timmermann H, Fouquet D, Weber A, Ivers-Tiffée E, Hennings U, Reimert R. Internal Reforming of Methane at Ni/YSZ and Ni/CGO SOFC Cermet Anodes. Fuel Cells 2006;6:307–13. doi:10.1002/fuce.200600002.
[48] Ahmed K, Foger K. Kinetics of internal steam reforming of methane on Ni/YSZ-based anodes for solid oxide fuel cells. Catalysis Today 2000;63:479–87. doi:10.1016/S0920-5861(00)00494-6.
[49] Mansouri Z, Settar A, Khamane H. Computational investigation of heat load and secondary flows near tip region in a transonic turbine rotor with moving shroud. Applied Thermal Engineering 2018;136:141–51. doi:10.1016/j.applthermaleng.2018.03.012.
[50] Djedai H, Mdouki R, Mansouri Z, Aouissi M. Numerical investigation of three-dimensional separation control in an axial compressor cascade. International Journal of Heat and Technology 2017;35:657–662.
[51] Rahimi-Gorji M, Ghajar M, Kakaee A-H, Ganji DD. Modeling of the air conditions effects on the power and fuel consumption of the SI engine using neural networks and regression. Journal of the Brazilian Society of Mechanical Sciences and Engineering 2017;39:375–384.
[52] Rahimi-Gorji M, Gorji TB, Gorji-Bandpy M. Details of regional particle deposition and airflow structures in a realistic model of human tracheobronchial airways: two-phase flow simulation. Computers in Biology and Medicine 2016;74:1–17.
[53] Mansouri Z, Aouissi M, Boushaki T. Detached eddy simulation of high turbulent swirling reacting flow in a premixed model burner. Combustion Science and Technology 2016;188:1777–1798.
[54] Mansouri Z, Boushaki T. Experimental and numerical investigation of turbulent isothermal and reacting flows in a non-premixed swirl burner. International Journal of Heat and Fluid Flow 2018;72:200–213.
[55] Khamane H, Azzi A, Mansouri Z. Numerical Investigation of Film-Cooling Effectiveness Downstream of a Micro Ramp. Computational Thermal Sciences: An International Journal 2018;10.
[56] Settar A, Nebbali R, Madani B, Abboudi S. Numerical study on the effects of the macropatterned active surfaces on the wall-coated steam methane reformer performances. International Journal of Hydrogen Energy 2016.

[57] Settar A, Abboudi S, Lebaal N. Effect of inert metal foam matrices on hydrogen production intensification of methane steam reforming process in wall-coated reformer. International Journal of Hydrogen Energy 2018. doi:10.1016/j.ijhydene.2018.04.215.